Universiteit
Leiden
The Netherlands

Warm and cold gas in low-mass protostars : Herschel Space Observatory and ground-based surveys

Yildiz, U

Citation

Yildiz, U. (2013, May 1). *Warm and cold gas in low-mass protostars : Herschel Space Observatory and ground-based surveys*. Retrieved from https://hdl.handle.net/1887/20855

Version:	Not Applicable (or Unknown)
License:	Leiden University Non-exclusive license
Downloaded from:	https://hdl.handle.net/1887/20855

Note: To cite this publication please use the final published version (if applicable).

Cover Page

Universiteit Leiden

The handle http://hdl.handle.net/1887/20855 holds various files of this Leiden University dissertation.

Author: Yildiz, Umut
Title: Warm and cold gas in low-mass protostars : Herschel Space Observatory and ground-based surveys
Issue Date: 2013-05-01

5

APEX-CHAMP$^+$ high-J CO observations of low–mass young stellar objects: IV. Mapping survey of low-mass protostars

Umut A. Yıldız, Ewine F. van Dishoeck, Lars E. Kristensen, Tim A. van Kempen, Michiel R. Hogerheijde, Agata Karska, Friedrich Wyrowski, Nienke van der Marel, Arnaud Belloche, Rolf Güsten

In preparation

Abstract

CONTEXT: During the embedded stage of star formation, the envelope mass and bipolar outflow characteristics undergo significant evolution. The outflow is the dominant feedback agent, and its evolution reflects the accretion processes of the forming star.

AIMS: Our aim is to quantify the outflow force for a large sample of sources in a consistent manner to determine the evolution of outflow activity integrated over the lifetime of the protostar. The outflow activity is then compared with other energetic parameters of the system to search for correlations and evolutionary trends.

METHODS: Large-scale maps of 26 young stellar objects which are part of the *Herschel* WISH key program are obtained using the CHAMP$^+$ instrument on the Atacama Pathfinder EXperiment (^{12}CO and ^{13}CO 6–5; E_{up}~100 K), together with the HARP-B instrument on the James Clerk Maxwell Telescope (^{12}CO and ^{13}CO 3–2; E_{up}~30 K). The maps have high spatial resolution, particularly the CO 6–5 maps taken with a 9″ beam, resolving the morphology of the outflows. These maps are analyzed using the same methods to determine outflow parameters and the results are compared with higher-J CO lines obtained with *Herschel*.

RESULTS: All sources in our sample show outflow activity via CO line wings. One of the key parameters, the outflow force, F_{CO}, is measured and correlations with other physical parameters are sought. F_{CO} versus L_{bol} plots show that Class 0 sources have more powerful outflows than the Class I sources, even if their luminosities are comparable. Overall, the various outflow parameters indicate reduced outflow activity with evolutionary stage, consistent with previous studies. F_{CO} is directly proportional to M_{env} and $M_{outflow}$, indicating that higher outflow forces require higher envelope masses and involve higher outflow masses. Comparison of the CO 6–5 results with H_2O lines observed with HIFI and high-J CO lines probed by PACS, both tracing currently shocked gas, shows that the two components are still linked, even though the transitions do not probe the same gas component. The link does not extend down to CO 3–2. The conclusion is that CO 6–5 depends on the shock characteristics (pre-shock density and velocity), whereas CO 3–2 is more sensitive to conditions in the surrounding environment (density).

5.1 Introduction

During the early phases of star-formation, material surrounding the newly forming star accretes onto the forming protostar. At the same time, it launches winds or jets at supersonic speeds from the star-disk system, which sweep up surrounding envelope material in large bipolar outflows. The material is accelerated and pushed to distances of several tens of thousands of AU, and these outflows play a pivotal role in the physics and chemistry of the star-forming cores (Snell et al. 1980, Goldsmith et al. 1984, Lada 1987, Greene et al. 1994, Bachiller & Tafalla 1999, Arce & Sargent 2006, Tafalla et al. 2013). The youngest protostars have highly collimated outflows driven by jets, whereas at later stages wide-angle winds drive less collimated outflows. However, there is still not a general consensus to explain the launching mechanisms and nature of these outflows (Arce et al. 2007).

The goal of this chapter is to investigate how the outflow activity varies with evolution and how this compares with other measures of the accretion processes. The outflows show the integrated activity over the entire lifetime of the protostar, which could be the result of multiple accretion and ejection events. It is important to distinguish this probe from the current accretion rate, as reflected for example in the luminosity of the source, in order to understand the accretion history. The well-known "luminosity problem" in low-mass star-formation indicates that protostars are underluminous compared to theoretical models (Kenyon et al. 1990, Evans et al. 2009, Enoch et al. 2009, Dunham et al. 2013). One of the possible resolutions to this problem is that of "episodic accretion", in which the star builds up through short bursts of rapid accretion over long periods of time rather than continuous steady-state accretion. An accurate and consistent quantification of outflow properties such as the outflow force and mass is key to investigate this problem.

CO outflows have been observed in the last few decades in many sources, but those observations were mainly done via lower-J CO rotational transitions ($J_u \leq 3$) which probe colder swept-up or entrained gas ($T \sim 50$–100 K) (e.g., Bachiller et al. 1990, Blake et al. 1995, Bontemps et al. 1996, Tafalla et al. 2000, Curtis et al. 2010b, and many others). One of the key parameters that is used for the evolutionary studies of star formation is the "outflow force", which is known as the strength of an outflow and defined similar to the centripetal force. These studies conclude that the outflow force correlates well with bolometric luminosity, L_{bol}, a correlation which holds over several orders of magnitude. Furthermore, the outflow force from Class 0 sources is stronger than for Class I sources, indicating an evolutionary trend. The correlations, however, often show some degree of scatter, typically more than an order of magnitude in F_{CO} for any value of L_{bol}. Some of the uncertainties in these studies include the opacity in the line wings, the adopted inclination angle and cloud contamination at low outflow velocities. Comparison with other outflow tracers such as water now being observed with the *Herschel* Space Observatory is further complicated by the fact that the various studies use different analysis methods to derive outflow parameters from low-J CO maps.

Tracing warmer gas ($T \gtrsim 100$ K) in the envelope or in the surroundings requires obser-

vations of higher-J transitions of CO, e.g., $J_u \geq 5$, for which ground-based telescopes demand excellent weather conditions on dry observing sites. The CHAMP+ instrument, mounted on the Atacama Pathfinder EXperiment (APEX) at an altitude of 5100 meters on Cerro Chajnantor (Güsten et al. 2008), has a 650/850 GHz 2×7 pixel array receiver (Kasemann et al. 2006), which is ideally suited to observe higher-J CO transitions and efficiently map extended sources. Broad line wings of CO 6–5 (E_u/k=115 K) suffer less from opacity effects than CO 3–2 (E_u/k=33 K) (van Kempen et al. 2009a, Yıldız et al. 2012). Moreover, the ambient cloud contribution is smaller for these higher-J transitions, except close to the source position, where the protostellar envelope may still contribute. Even higher-J CO lines up to J_u=50 are now routinely observed with the *Herschel* (Pilbratt et al. 2010) and provide information on the shocked gas in the *Herschel* beam (Herczeg et al. 2012, Manoj et al. 2013, Goicoechea et al. 2012, Benedettini et al. 2012, Nisini et al. 2013, Karska et al. 2013).

In this chapter, we present an APEX-CHAMP+ survey of 26 low-mass young stellar objects (YSOs), which were mapped in CO J = 6–5 and isotopologues in order to trace their outflow activity, following van Kempen et al. (2009a,b) and Yıldız et al. (2012), papers I, II and III in this series. These data complement our earlier surveys at lower frequency of CO and other molecules with the James Clerk Maxwell Telescope (JCMT) and APEX (e.g., Jørgensen et al. 2002, 2004, van Kempen et al. 2009c). The same sources are covered in the *Herschel* key project, "Water in star-forming regions with Herschel" (WISH; van Dishoeck et al. 2011). Many of the sources are also included in the "Dust, Ice and Gas in Time" program (DIGIT; PI: N. Evans; Green et al. 2013; subm.).

The YSOs in our sample cover both the deeply embedded Class 0 stage as well as the less embedded Class I stage (André et al. 2000, Robitaille et al. 2006). The full data set covering many sources allows us to address important characteristics of YSOs through the evolution from Class 0 to Class I in a more accurate manner. These characteristics can be inferred from their different morphologies, outflow forces, envelope masses, etc. and eventually be compared with evolutionary models.

The study presented here is complementary to that of Yıldız et al. (2013; subm.), where only the source position was studied in CO transitions from J = 1–0 to 10–9 (E_{up}~300 K), and trends with evolution were examined. The results obtained from the ^{12}CO maps are complemented by ^{13}CO 6–5 data of the same sources, with the narrower ^{13}CO 6–5 lines found to be a good tracer of the UV photon-heated gas (Spaans et al. 1995, van Kempen et al. 2009b, Yıldız et al. 2012). However, this analysis if beyond the scope of this chapter, and the ^{13}CO maps are only presented in Figs. 5.15 and 5.16 in the Additional Materials.

The outline of the chapter is as follows. In Section 5.2, the observations and the telescopes where the data have been obtained are described. In Section 5.3, physical parameters obtained from molecular outflows are given. In Section 5.4, these results are discussed, and conclusions from this work are presented in Sect. 5.5.

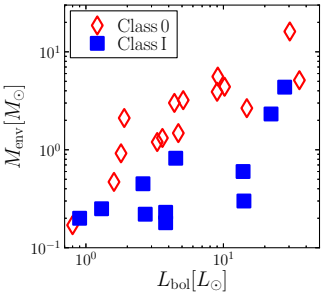

Figure 5.1 – Bolometric luminosity, $L_{\rm bol}$, versus envelope mass, $M_{\rm env}$, for the surveyed sources. Red triangles and blue squares indicate Class 0 and Class I sources, respectively.

5.2 Sample and observations

5.2.1 Sample

The sample selection criteria with the coordinates and other basic information of the source list are presented in van Dishoeck et al. (2011) with updates in Kristensen et al. (2012), and is the same as the sample presented in Yıldız et al. (2013; subm.). It consists of 15 Class 0 and 11 Class I embedded protostellar sources located in the Perseus, Ophiuchus, Taurus, and Serpens molecular clouds. The average distance is 200 pc, with a maximum distance of 450 pc.

Figure 5.1 presents the envelope mass ($M_{\rm env}$) as a function of bolometric luminosity ($L_{\rm bol}$) for all sources. The envelope mass is obtained from dust modelling, which is measured either at the $T_{\rm dust}$=10 K radius or at the n=10^4cm^{-3} radius, depending on which is smaller (Kristensen et al. 2012). Class 0 sources and Class I sources are well separated in the diagram, with the Class 0 sources having higher envelope masses. The parameters are taken from Kristensen et al. (2012) based on fits of the spectral energy distributions (SEDs) including new *Herschel*-PACS fluxes, as well as the spatial extent of the envelopes observed at submillimeter wavelengths. This type of correlation diagram has been put forward by Saraceno et al. (1996) and subsequently used as an evolutionary diagram for embedded YSOs with lower envelope masses representing later stages (e.g., Bontemps et al. 1996, Hogerheijde et al. 1998, Hatchell et al. 2007). In our sample, envelope masses range from 0.04 $M_\odot$ (Elias 29) to 16 $M_\odot$ (SMM1) and the luminosities range from 0.8 $L_\odot$ (Ced110IRS1) to 35.7 $L_\odot$ (IRAS 2A). The large range of masses and luminosities makes the sample well suited for statistical studies and trends with various source parameters. The range of luminosities studied is similar to that of Bontemps et al. (1996), ~0.5 to 15 $L_\odot$, but our sample is more weighted toward higher luminosities.

5.2.2 Observations

Molecular line observations of CO in the J=6–5 transitions were done with the 12-m submillimeter Atacama Pathfinder EXperiment, APEX[1] (Güsten et al. 2008) at Llano de Chajnantor in Chile, whereas the J=3–2 transition was primarily observed at the 15-m James Clerk Maxwell Telescope, JCMT[2] at Mauna Kea, Hawaii.

APEX: ^{12}CO and ^{13}CO 6–5 maps of the survey were obtained with the CHAMP+ instrument on APEX between June 2007 and September 2012. The CHAMP+ instrument consists of two heterodyne receiver arrays, each with seven pixel detector elements for simultaneous operations in the 620–720 GHz and 780–950 GHz frequency ranges (Kasemann et al. 2006, Güsten et al. 2008). The observational procedures are explained in detail in van Kempen et al. (2009a,b,c) and Yıldız et al. (2012). Simultaneous observations were done with the following settings of the lower and higher frequency bands: ^{12}CO 6–5 with ^{12}CO 7–6; ^{13}CO 6–5 with [C I] 2–1. ^{12}CO maps cover the entire outflow extent with a few exceptions (L1527 and L1551-IRS5), whereas ^{13}CO maps cover only a ∼100″×100″ region around the central source position. L1157 is part of the WISH survey, but because it is not accessible from APEX (dec = +68°), no CO 6–5 data are presented.

The APEX beam size is ∼9″ (∼1800 AU for a source at 200 pc) at 691 GHz. The observations were done using position-switching toward an emission-free reference position. The CHAMP+ instrument uses the Fast Fourier Transform Spectrometer (FFTS) backend (Klein et al. 2006) for all seven pixels with a resolution of 0.12 MHz (0.052 km s^{-1} at 691 GHz). Typical *rms* for the CO 6–5 and ^{13}CO 6–5 observations are ∼0.2 K in 0.2 km s^{-1} channels. Apart from the high-J CO observations, some of the 3–2 line observations were also conducted with APEX for a few southern sources, e.g., DK Cha, Ced110 IRS4, and HH 46 (van Kempen et al. 2009c).

JCMT: Fully sampled on-the-fly maps of ^{12}CO and ^{13}CO 3–2 were obtained using the HARP-B instrument mounted on the JCMT. HARP-B consists of 16 SIS detectors with 4×4 pixel elements of 15″ each at 30″ separation. Most of the maps were obtained through our own dedicated proposals, with a subset obtained from the JCMT public archive[3].

The data were acquired on the $T_{\rm A}^*$ antenna temperature scale and were converted to main-beam brightness temperatures $T_{\rm MB} = T_{\rm A}^*/\eta_{\rm MB}$ using the beam efficiencies ($\eta_{\rm MB}$). The CHAMP+ beam efficiencies were taken from the CHAMP+ website[4] and forward ef-

[1] This publication is based on data acquired with the Atacama Pathfinder Experiment (APEX). APEX is a collaboration between the Max-Planck-Institut für Radioastronomie, the European Southern Observatory, and the Onsala Space Observatory.

[2] The JCMT is operated by The Joint Astronomy Centre on behalf of the Science and Technology Facilities Council of the United Kingdom, the Netherlands Organisation for Scientific Research, and the National Research Council of Canada.

[3] This research used the facilities of the Canadian Astronomy Data Centre operated by the National Research Council of Canada with the support of the Canadian Space Agency.

[4] http:www.mpifr.de/div/submmtech/heterodyne/champplus/champ_efficiencies.15-10-09.html

ficiencies are 0.95 in all observations. The various beam efficiencies are all stated in Yıldız et al. (2013; subm.) and are typically ~ 0.5 (see also the thesis Appendix). The JCMT beam efficiencies were taken from the JCMT Efficiencies Database[5], and 0.63 is used for all HARP-B observations. Calibration errors are estimated to be ~20% for both telescopes. Typical *rms* noise levels of the 3–2 data are from 0.05 K to 0.1 K in 0.2 km s^{-1} channels.

For the data reduction and analysis, the "Continuum and Line Analysis Single Dish Software", `CLASS` program, which is part of the GILDAS software[6], is used. In particular, linear baselines were subtracted from all spectra. ^{12}CO and ^{13}CO 6–5 and 3–2 line profiles of the central source positions of all the sources in the sample are presented in Yıldız et al. (2013; subm.).

5.2.3 ^{12}CO maps

All spectra are binned to a 0.5 km s^{-1} velocity resolution for analyzing the outflows. The intensities of the blue and red outflow lobes are calculated by integrating the blue and red emission in each of the spectra separately, where the integration limits are carefully selected for each source by using their CO 6–5 lines (see Fig. 5.10). First, in order to find the inner velocity limit ($V_{\rm in}$), a spatial region not part of the outflow is selected. The spectra in this region are averaged to determine the narrow line emission coming from the envelope and surrounding cloud and $V_{\rm in}$ is estimated. Second, the outer velocity limits ($V_{\rm out}$) are determined from a representative high S/N spectrum inside each of the blue and red outflow lobes. The outer velocity limits are selected as the velocity where the emission in the spectrum goes down to the 1σ limit. Finally, the blue- and red-shifted integrated intensity is measured by integrating over these velocity limits across the entire map.

The resulting maps of all sources are presented in Figs. 5.2 and 5.3, where blue and red contours show the blue- and red-shifted outflow lobes, respectively. A few maps only cover the central ~ $2'\times2'$, specifically the four Class 0 sources IRAS 2A, L723mm, L1527, and the two Class I sources Elias 29 and L1551IRS5. Source-by-source outflow and intensity maps obtained from the 6–5 and 3–2 data are presented in Figs. 5.11–5.14 in the Additional Materials.

5.2.4 ^{13}CO maps

The ^{13}CO 6–5 and 3–2 transitions were mapped around the central ~ $1'\times1'$, corresponding to typically 10^4 AU × 10^4 AU. The total integrated intensity is measured for all the sources, where the limits correspond to the velocities at which the emission reaches down to 1σ. ^{13}CO maps can be used to quantify the UV-heated gas around the outflow cavity

[5] http://www.jach.hawaii.edu/JCMT/spectral_line/Standards/eff_web.html
[6] http:www.iram.fr/IRAMFR/GILDAS

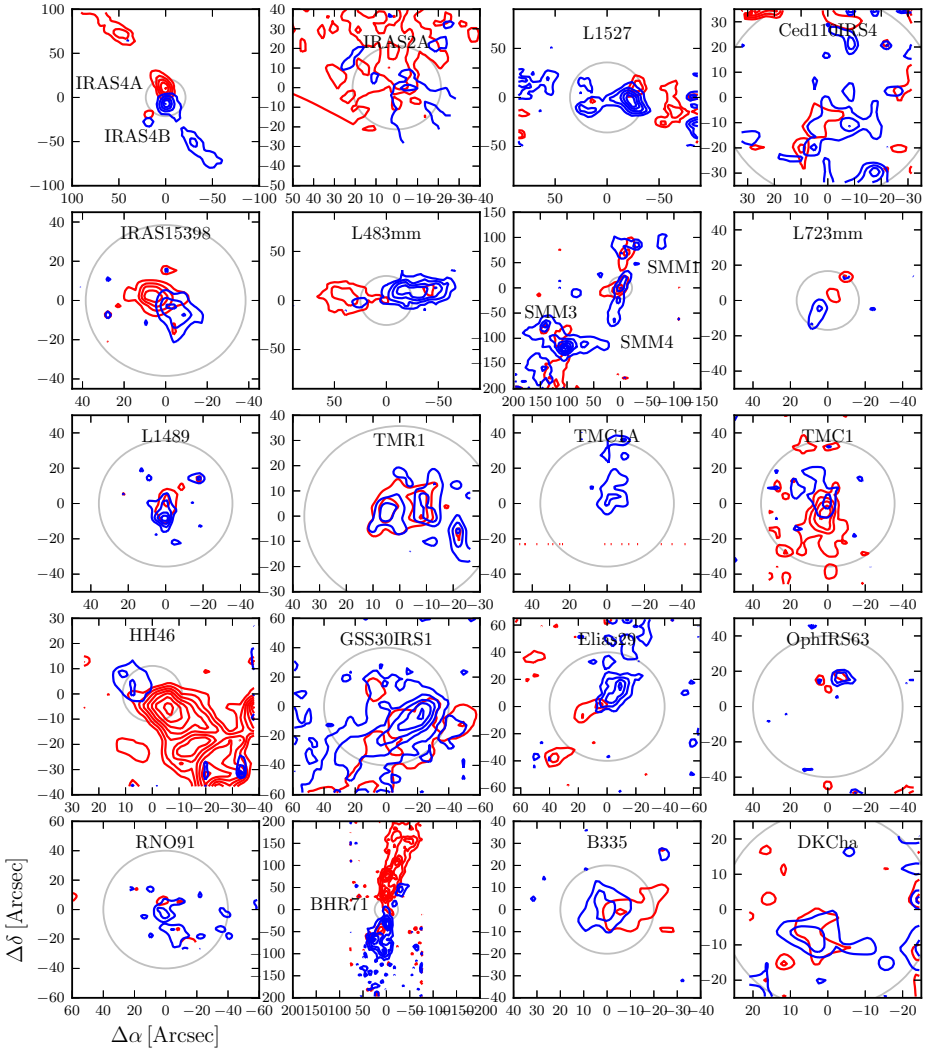

Figure 5.2 – Overview of the outflows traced by the ^{12}CO 6–5 observations with the APEX-CHAMP+ instrument. Contour levels are given in Table 5.5 and the source is located at (0,0) in each map, with the exception of the maps of NGC1333-IRAS4A and 4B, and Ser-SMM1, SMM3 and SMM4, which are located in the same maps, respectively. The circle in each plot corresponds to a region of 5000 AU radius at the distance of each source.

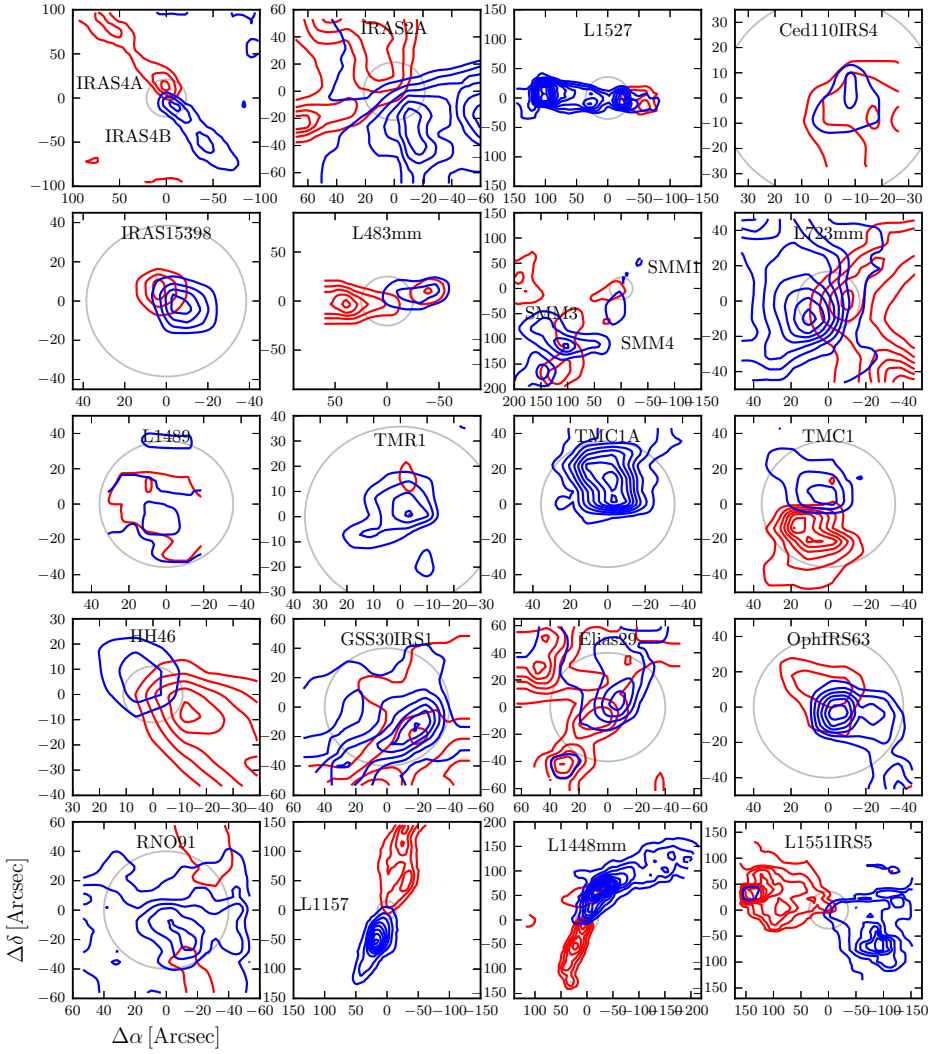

Figure 5.3 – Overview of the entire set of outflows traced by the ^{12}CO 3–2 observations with the JCMT and APEX. Contour levels are given in Table 5.5 and the source is located at (0,0) in each map, with the exception of the maps of NGC1333-IRAS4A and 4B, and Ser-SMM1, SMM3 and SMM4, which are located in the same maps, respectively. The circle in each plot corresponds to a region of 5000 AU radius at the distance of each source.

walls as demonstrated by Yıldız et al. (2012). All maps are presented in Figs. 5.15 and 5.16 in the Additional materials.

5.3 Results

5.3.1 Outflow morphology

All sources show strong outflow activity in both CO transitions, J = 3–2 and 6–5, as evident from both the maps and spectra (Figs. 5.2, 5.3, and Figs. 5.10–5.14). The advantage of the CO 6–5 maps is that they have higher spatial resolution by a factor of two than the CO 3–2 maps. On the other hand, the CO 3–2 maps have the advantage of higher S/N than the CO 6–5 maps by typically a factor of 4 in antenna temperature.

Most sources show a clear blue-red bipolar structure. In a few cases only one lobe is observed. Particular examples are TMC1A, which shows no red-shifted outflow lobe, and HH 46, which has only a very small blue-shifted outflow lobe. One explanation is that these sources are at the edge of the cloud and that there is no cloud material to run into (van Kempen et al. 2009b). For L723mm, IRAS 2A and BHR71, two outflows are driven by two independent protostars (Lee et al. 2002, Parise et al. 2006) and both outflows are detected in our CO 3–2 maps. In CO 6–5, only one outflow shows up toward L723, whereas both outflows are seen towards IRAS2A and BHR71.

Visual inspection shows that the Class 0 outflows are more collimated than their Class I counterparts as expected (e.g., Arce et al. 2007). The length of the outflows can be quantified for most of the sources. $R_{\rm CO}$ is defined as the total outflow extent assuming that the outflows are fully covered in the map. $R_{\rm CO}$ is measured separately for the blue and red outflow lobes as the projected size, with sometimes significantly different values. In some sources, e.g., Ced110 IRS4, Elias 29, and DK Cha, the blue and red outflow lobes overlap, likely because the outflow is observed nearly pole on. In those cases, $R_{\rm CO}$ could not be properly estimated and the estimated value is a lower limit.

5.3.2 Outflow parameters

In the following, different outflow parameters, including mass, force and luminosity, are measured. These parameters have previously been determined from lower-J lines for several young stellar objects (e.g., Cabrit & Bertout 1992, Bontemps et al. 1996, Hogerheijde et al. 1998, Hatchell et al. 2007) and more recently from CO 6–5 by van Kempen et al. (2009b) and Yıldız et al. (2012) for a small subset of the sources presented here. All parameters are listed in Tables 5.1–5.3.

Table 5.1 – Outflow properties of the red and blue outflow lobes of YSOs.

Source	Trans.	Inclination [°]	Lobe	V_{max} [a] [km s^{-1}]	R_{CO} [a] [AU]	t_{dyn} [a,b] [10^3 yr]	$M_{outflow}$ [c,d] [$M_\odot$]	$\dot{M}$ [d,e] [$M_\odot$ yr^{-1}]	F_{CO} [d,f] [$M_\odot$ yr^{-1}km s^{-1}]	L_{kin} [d,g] [$L_\odot$]
IRAS2A	CO 3–2	70	Blue	23	3.3×10^{4}	6.7	2.4×10^{-1}	3.6×10^{-5}	8.3×10^{-4}	1.6×10^{0}
			Red	15	3.3×10^{4}	10.2	7.7×10^{-1}	7.6×10^{-5}	1.2×10^{-3}	1.5×10^{0}
IRAS4A	CO 6–5	50	Blue	23	2.5×10^{4}	5.1	5.6×10^{-2}	1.1×10^{-5}	2.6×10^{-4}	4.8×10^{-1}
			Red	23	3.5×10^{4}	7.3	3.7×10^{-1}	5.1×10^{-5}	1.2×10^{-3}	2.2×10^{0}
	CO 3–2	50	Blue	23	2.5×10^{4}	5.1	3.4×10^{-2}	6.6×10^{-6}	1.5×10^{-4}	2.9×10^{-1}
			Red	23	3.5×10^{4}	7.3	2.5×10^{-1}	3.5×10^{-5}	7.9×10^{-4}	1.5×10^{0}
IRAS4B	CO 6–5	10	Blue	18	3.5×10^{3}	0.9	2.2×10^{-3}	2.4×10^{-6}	4.3×10^{-5}	6.3×10^{-2}
			Red	16	2.4×10^{3}	0.7	8.4×10^{-3}	1.2×10^{-5}	1.9×10^{-4}	2.4×10^{-1}
	CO 3–2	10	Blue	23	3.5×10^{3}	0.7	4.0×10^{-4}	5.5×10^{-7}	1.3×10^{-5}	2.4×10^{-2}
			Red	15	2.4×10^{3}	0.8	4.2×10^{-3}	5.6×10^{-6}	8.3×10^{-5}	1.0×10^{-1}
L1527	CO 6–5	70	Blue	9	1.5×10^{4}	8.5	3.0×10^{-2}	3.5×10^{-6}	3.0×10^{-5}	2.1×10^{-2}
			Red	7	1.1×10^{4}	7.5	8.7×10^{-2}	1.2×10^{-5}	8.2×10^{-5}	4.8×10^{-2}
	CO 3–2	70	Blue	7	3.2×10^{4}	20.6	6.8×10^{-2}	3.3×10^{-6}	2.4×10^{-5}	1.5×10^{-2}
			Red	11	1.1×10^{4}	4.8	4.5×10^{-2}	9.4×10^{-6}	1.1×10^{-4}	9.6×10^{-2}
Ced110IRS4	CO 6–5	30	Blue	10	3.8×10^{3}	1.7	2.8×10^{-4}	1.6×10^{-7}	1.7×10^{-6}	1.4×10^{-3}
			Red	11	3.8×10^{3}	1.6	1.4×10^{-3}	8.7×10^{-7}	9.4×10^{-6}	8.3×10^{-3}
BHR71	CO 6–5	70	Blue	16	4.4×10^{4}	13.4	6.0×10^{-1}	4.5×10^{-5}	6.9×10^{-4}	8.8×10^{-1}
			Red	16	4.0×10^{4}	11.5	3.2×10^{-1}	2.7×10^{-5}	4.5×10^{-4}	6.1×10^{-1}
IRAS15398	CO 6–5	50	Blue	12	2.6×10^{3}	1.1	7.3×10^{-4}	6.9×10^{-7}	7.9×10^{-6}	7.4×10^{-3}
			Red	11	2.6×10^{3}	1.1	4.4×10^{-3}	3.9×10^{-6}	4.2×10^{-5}	3.8×10^{-2}
	CO 3–2	50	Blue	13	3.2×10^{3}	1.2	7.9×10^{-4}	6.5×10^{-7}	8.2×10^{-6}	8.5×10^{-3}
			Red	12	2.0×10^{3}	0.8	1.3×10^{-3}	1.7×10^{-6}	2.0×10^{-5}	2.0×10^{-2}
L483mm	CO 6–5	70	Blue	9	1.2×10^{4}	6.7	4.0×10^{-2}	6.0×10^{-6}	5.1×10^{-5}	3.6×10^{-2}
			Red	7	1.0×10^{4}	7.0	1.3×10^{-1}	1.8×10^{-5}	1.2×10^{-4}	6.9×10^{-2}
	CO 3–2	70	Blue	13	1.4×10^{4}	5.2	4.3×10^{-3}	8.2×10^{-7}	1.0×10^{-5}	1.1×10^{-2}
			Red	13	1.0×10^{4}	3.7	6.5×10^{-2}	1.7×10^{-5}	2.2×10^{-4}	2.4×10^{-1}

Notes: [a]Velocities and extent are not corrected for inclination. [b]Dynamical timescale. [c]Constant temperatures of 100 K and 75 K are assumed for the CO 6–5 and CO 3–2 calculations. [d]Corrected for inclination as explained in Sect. 5.3.2.2. [e]Mass outflow rate [f]Outflow force [g]Kinetic luminosity.

Table 5.2 – Outflow properties of the red and blue outflow lobes of YSOs.

Source	Trans.	Inclination [°]	Lobe	V_{max}[a] [km s^{-1}]	R_{CO}[a] [AU]	t_{dyn}[a,b] [10^3 yr]	$M_{outflow}$[c,d] [M$_\odot$]	$\dot{M}$[d,e] [M$_\odot$ yr^{-1}]	F_{CO}[d,f] [M$_\odot$ yr^{-1}km s^{-1}]	L_{kin}[d,g] [L$_\odot$]
SMM1	CO 6–5	50	Blue	17	3.4×10^{4}	9.6	8.6×10^{-2}	8.9×10^{-6}	1.5×10^{-4}	2.1×10^{-1}
			Red	21	1.8×10^{4}	4.2	1.5×10^{-1}	3.5×10^{-5}	7.1×10^{-4}	1.2×10^{0}
	CO 3–2	50	Blue	19	3.4×10^{4}	8.6	1.1×10^{-1}	1.3×10^{-5}	2.4×10^{-4}	3.8×10^{-1}
			Red	21	1.8×10^{4}	4.2	1.6×10^{-1}	3.7×10^{-5}	7.5×10^{-4}	1.3×10^{0}
SMM4	CO 6–5	30	Blue	19	3.4×10^{4}	8.8	1.7×10^{-1}	2.0×10^{-5}	3.6×10^{-4}	5.5×10^{-1}
			Red	12	3.4×10^{4}	13.6	3.0×10^{-1}	2.2×10^{-5}	2.6×10^{-4}	2.6×10^{-1}
	CO 3–2	30	Blue	19	3.4×10^{4}	8.6	2.4×10^{-1}	2.8×10^{-5}	5.3×10^{-4}	8.2×10^{-1}
			Red	12	3.4×10^{4}	14.2	5.5×10^{-1}	3.9×10^{-5}	4.5×10^{-4}	4.2×10^{-1}
SMM3	CO 6–5	50	Blue	20	4.6×10^{3}	1.1	3.3×10^{-2}	3.0×10^{-5}	6.1×10^{-4}	1.0×10^{0}
			Red	12	4.6×10^{3}	1.8	5.5×10^{-2}	3.1×10^{-5}	3.9×10^{-4}	3.9×10^{-1}
	CO 3–2	50	Blue	21	4.6×10^{3}	1.0	4.0×10^{-2}	3.9×10^{-5}	8.1×10^{-4}	1.4×10^{0}
			Red	12	4.6×10^{3}	1.9	8.9×10^{-2}	4.7×10^{-5}	5.4×10^{-4}	5.1×10^{-1}
B335	CO 6–5	70	Blue	12	6.2×10^{3}	2.4	5.4×10^{-3}	2.2×10^{-6}	2.8×10^{-5}	2.8×10^{-2}
			Red	7	7.5×10^{3}	5.4	6.6×10^{-2}	1.2×10^{-5}	8.1×10^{-5}	4.4×10^{-2}
L723mm	CO 6–5	50	Blue	13	1.2×10^{4}	4.4	2.8×10^{-2}	6.5×10^{-6}	8.4×10^{-5}	9.0×10^{-2}
			Red	11	1.2×10^{4}	5.3	9.4×10^{-2}	1.8×10^{-5}	1.9×10^{-4}	1.7×10^{-1}
	CO 3–2	50	Blue	19	2.1×10^{4}	5.4	7.6×10^{-2}	1.4×10^{-5}	2.7×10^{-4}	4.1×10^{-1}
			Red	16	1.8×10^{4}	5.4	2.6×10^{-1}	4.8×10^{-5}	7.6×10^{-4}	9.8×10^{-1}
L1157	CO 3–2	70	Blue	10	4.4×10^{4}	20.0	2.4×10^{-1}	1.2×10^{-5}	1.3×10^{-4}	1.1×10^{-1}
			Red	15	5.2×10^{4}	16.0	9.7×10^{-1}	6.1×10^{-5}	9.4×10^{-4}	1.2×10^{0}
L1489	CO 6–5	50	Blue	12	2.1×10^{3}	0.9	3.7×10^{-4}	4.3×10^{-7}	4.9×10^{-6}	4.6×10^{-3}
			Red	7	2.1×10^{3}	1.5	3.7×10^{-3}	2.5×10^{-6}	1.7×10^{-5}	9.5×10^{-3}
	CO 3–2	50	Blue	15	2.1×10^{3}	0.7	1.2×10^{-3}	1.8×10^{-6}	2.7×10^{-5}	3.2×10^{-2}
			Red	10	2.1×10^{3}	1.0	9.8×10^{-3}	9.6×10^{-6}	9.4×10^{-5}	7.6×10^{-2}
L1551IRS5	CO 3–2	70	Blue	13	1.7×10^{4}	6.3	2.2×10^{-2}	3.5×10^{-6}	4.5×10^{-5}	4.6×10^{-2}
			Red	11	1.7×10^{4}	7.4	9.6×10^{-2}	1.3×10^{-5}	1.4×10^{-4}	1.2×10^{-1}

Notes: [a]Velocities and extent are not corrected for inclination. [b]Dynamical timescale. [c]Constant temperatures of 100 K and 75 K are assumed for the CO 6–5 and CO 3–2 calculations. [d]Corrected for inclination as explained in Sect. 5.3.2.2. [e]Mass outflow rate [f]Outflow force [g]Kinetic luminosity.

Table 5.3 – Outflow properties of the red and blue outflow lobes of the YSOs.

Source	Trans.	Inclination [°]	Lobe	V_{max} [a] [km s^{-1}]	R_{CO} [a] [AU]	t_{dyn} [a,b] [10^3 yr]	$M_{outflow}$ [c] [M$_\odot$]	$\dot{M}$ [a,e] [M$_\odot$ yr^{-1}]	F_{CO} [a,f] [M$_\odot$ yr^{-1}km s^{-1}]	L_{kin} [a,g] [L$_\odot$]
TMR1	CO 6–5	50	Blue	10	4.9×10^{3}	2.4	8.5×10^{-4}	3.5×10^{-7}	3.3×10^{-6}	2.6×10^{-3}
			Red	6	4.9×10^{3}	4.1	4.4×10^{-3}	1.1×10^{-6}	6.2×10^{-6}	2.9×10^{-3}
	CO 3–2	50	Blue	11	1.4×10^{4}	6.1	2.0×10^{-3}	3.3×10^{-7}	3.6×10^{-6}	3.2×10^{-3}
			Red	4	3.5×10^{3}	4.5	7.8×10^{-3}	1.7×10^{-6}	6.5×10^{-6}	2.0×10^{-3}
TMC1A	CO 3–2	50	Blue	19	5.6×10^{3}	1.4	3.2×10^{-3}	2.3×10^{-6}	4.5×10^{-5}	7.0×10^{-2}
			Red	7	1.7×10^{3}	1.1	2.7×10^{-3}	2.6×10^{-6}	1.9×10^{-5}	1.1×10^{-2}
TMC1	CO 6–5	50	Blue	12	2.8×10^{3}	1.2	6.1×10^{-4}	5.3×10^{-7}	6.1×10^{-6}	5.7×10^{-3}
			Red	15	2.8×10^{3}	0.9	5.5×10^{-3}	6.2×10^{-6}	9.2×10^{-5}	1.1×10^{-1}
	CO 3–2	50	Blue	16	3.5×10^{3}	1.1	8.2×10^{-4}	7.7×10^{-7}	1.2×10^{-5}	1.6×10^{-2}
			Red	17	2.1×10^{3}	0.6	5.2×10^{-3}	8.8×10^{-6}	1.5×10^{-4}	2.1×10^{-1}
HH46	CO 6–5	50	Blue	12	6.8×10^{3}	2.8	1.8×10^{-2}	6.6×10^{-6}	7.6×10^{-5}	7.2×10^{-2}
			Red	20	2.7×10^{4}	6.5	1.3×10^{-1}	2.0×10^{-5}	3.9×10^{-4}	6.4×10^{-1}
	CO 3–2	50	Blue	17	2.7×10^{4}	7.6	6.9×10^{-2}	9.0×10^{-6}	1.5×10^{-4}	2.1×10^{-1}
			Red	6	6.8×10^{3}	5.8	4.1×10^{-1}	7.0×10^{-5}	3.8×10^{-4}	1.7×10^{-1}
DKCha	CO 6–5	10	Blue	9	1.8×10^{3}	0.9	1.8×10^{-4}	2.0×10^{-7}	1.8×10^{-6}	1.4×10^{-3}
			Red	9	1.8×10^{3}	0.9	2.4×10^{-4}	2.5×10^{-7}	2.2×10^{-6}	1.6×10^{-3}
GSS30IRS1	CO 6–5	30	Blue	19	1.5×10^{4}	3.8	1.0×10^{-2}	2.6×10^{-6}	4.8×10^{-5}	7.3×10^{-2}
			Red	17	1.5×10^{4}	4.3	5.9×10^{-2}	1.4×10^{-5}	2.2×10^{-4}	3.0×10^{-1}
	CO 3–2	30	Blue	14	1.5×10^{4}	5.1	8.4×10^{-3}	1.7×10^{-6}	2.3×10^{-5}	2.7×10^{-2}
			Red	17	1.5×10^{4}	4.3	5.1×10^{-2}	1.2×10^{-5}	1.9×10^{-4}	2.6×10^{-1}
Elias29	CO 6–5	30	Blue	11	5.0×10^{3}	2.2	1.9×10^{-3}	8.6×10^{-7}	9.3×10^{-6}	8.3×10^{-3}
			Red	12	3.1×10^{3}	1.3	4.9×10^{-3}	3.9×10^{-6}	4.6×10^{-5}	4.4×10^{-2}
	CO 3–2	30	Blue	13	3.1×10^{3}	1.2	5.3×10^{-3}	4.6×10^{-6}	5.9×10^{-5}	6.1×10^{-2}
			Red	13	1.9×10^{3}	0.7	2.6×10^{-2}	3.7×10^{-5}	4.6×10^{-4}	4.8×10^{-1}
OphIRS63	CO 6–5	50	Blue	8	2.5×10^{3}	1.5	5.2×10^{-4}	3.5×10^{-7}	2.8×10^{-6}	1.8×10^{-3}
			Red	7	2.5×10^{3}	1.6	5.3×10^{-3}	3.2×10^{-6}	2.3×10^{-5}	1.4×10^{-2}
	CO 3–2	50	Blue	13	1.0×10^{4}	3.6	6.4×10^{-4}	1.8×10^{-7}	2.4×10^{-6}	2.6×10^{-3}
			Red	6	7.5×10^{3}	5.7	1.4×10^{-2}	2.5×10^{-6}	1.5×10^{-5}	7.7×10^{-3}

Notes: [a]Velocities and extent are not corrected for inclination. [b]Dynamical timescale. [c]Constant temperatures of 100 K and 75 K are assumed for the CO 6–5 and CO 3–2 calculations. Corrected for inclination as explained in Sect. 5.3.2.2. [e]Mass outflow rate [f]Outflow force [g]Kinetic luminosity.

5.3.2.1 Outflow mass

One of the most basic outflow parameters is the mass. The inferred mass only depends on three assumptions: the line opacity, the distribution of level populations, and the CO abundance with respect to H_2. In the following we assume that the line wings are optically thin, as has been demonstrated observationally for CO 6–5 for a few sources with massive outflows (e.g., NGC1333-IRAS4A, Yıldız et al. 2012). CO 3–2 emission is also assumed optically thin in the following, although that assumption may not be fully valid (see discussion below). The level populations are assumed to follow a Boltzmann distribution with a single temperature, $T_{\rm ex}$. Finally, the abundance ratio is taken as $[H_2/^{12}CO]=1.2\times10^4$.

The upper level column density per statistical weight in a single pixel (4.″5×4.″5 for CO 6–5, 7.″5×7.″5 for CO 3–2) is calculated as

$$\frac{N_{\rm u}}{g_{\rm u}} = \frac{\beta\nu^2 \int T_{\rm mb}{\rm d}V}{A_{\rm ul}\, g_{\rm u}} \,. \tag{5.1}$$

The constant β is $8\pi k/hc^3$=1937 cm^{-2} (GHz^2 K km)$^{-1}$. The remaining parameters are for the specific transition, where ν is the frequency, $A_{\rm ul}$ is the Einstein A coefficent and $g_{\rm u}=2J+1$.

The total CO column density in a pixel, $N_{\rm total}$, is

$$N_{\rm total} = \frac{N_{\rm u}}{g_{\rm u}} Q(T) e^{E_{\rm u}/kT_{\rm ex}} \,; \tag{5.2}$$

$Q(T)$ is the partition function corresponding to a specific excitation temperature, $T_{\rm ex}$, which is assumed as 75 K and 100 K for CO 3–2 and CO 6–5 observations, respectively (van Kempen et al. 2009b, Yıldız et al. 2012).

The mass is calculated as

$$M_{\rm outflow} = \mu_{\rm H_2}\, m_{\rm H}\, A \left[\frac{\rm H_2}{^{12}\rm CO}\right] \sum_j N_{{\rm total},j} \tag{5.3}$$

where the factor $\mu_{\rm H_2}$=2.8 includes the contribution of helium (Kauffmann et al. 2008) and $m_{\rm H}$ is the mass of the hydrogen atom. A is the surface area of one pixel j. The sum is over all outflow pixels. The effect of the assumed excitation temperature results in only ∼10% smaller mass at 100 K compared to 75 K.

5.3.2.2 Outflow velocity

The maximum outflow velocity, $V_{\rm max}$ is defined as $\|V_{\rm outflow}$-$V_{\rm LSR}\|$, the total velocity extent measured relative to the source velocity. $V_{\rm max}$ is estimated by selecting a representative spectrum from the blue and red outflow lobes separately, and its $FWZI$ (full-width at zero-intensity) is selected as the global value for $V_{\rm max}$ (Cabrit & Bertout 1992). Here, the

Table 5.4 – Inclination correction factors.

$i(^\circ)$	10	30	50	70
c_i	1.2	2.8	4.4	7.1

Notes: Line of sight inclinations, where i=0° indicates pole-on (Downes & Cabrit 2007, van der Marel et al. 2013; subm.).

zero-intensity level refers to the 1σ *rms* level in 0.5 km s^{-1} channels and the *FWZI* is measured from where the line profile first crosses this cutoff.

Two issues arise when determining $V_{\rm max}$: $V_{\rm max}$ is a function of the *rms* noise level and generally decreases with increasing *rms*. For noisy data, $V_{\rm max}$ may be underestimated compared to its true value. Second, if the outflow lobes are inclined, $V_{\rm max}$ suffers from projection effects. Both effects will increase the value of $V_{\rm max}$ if properly taken into account. As for the noise level, van der Marel et al. (2013; subm.) show that the effect on the outflow force may amount to a factor of a few at most and we ignore this issue in the following.

The second issue with determining $V_{\rm max}$ is the value of the inclination of the outflow lobes, which is difficult to estimate. The inclination is defined as the angle between the outflow direction and the line of sight (Cabrit & Bertout 1990, i=0° is pole on) and is determined based on the morphology in our high spatial resolution maps. Our estimates are listed in Tables 5.1– 5.3, and are consistent with the literature where available (Cabrit & Bertout 1992, Gueth et al. 1996, Bourke et al. 1997, Hogerheijde et al. 1997, Micono et al. 1998, Brown & Chandler 1999, Lommen et al. 2008, Tobin et al. 2008, van Kempen et al. 2010b).

Small radial velocities are expected for an outflow which lies in the plane of the sky. Therefore a correction factor for inclination, c_i is applied in the calculations. In Table 5.4, the correction factors from Downes & Cabrit (2007) are tabulated. The correction factors have been applied to the outflow rate, force and luminosity as listed in Tables 5.1–5.3.

5.3.2.3 Outflow force

One of the key outflow parameters is the outflow force, $F_{\rm CO}$. The best method for computing the outflow force is still debated and the results suffer from ill-constrained observational parameters, such as inclination, i. van der Marel et al. (2013; subm.) compare seven different methods proposed in the literature to calculate outflow forces. The "separation method" (see below) in their paper is found to be the preferred method, which is less affected by the observational biases. The method can also be applied to low spatial resolution observations or incomplete maps. Uncertainties are estimated to be a factor of a few.

In the following, the outflow force is calculated separately for the blue- and red-shifted

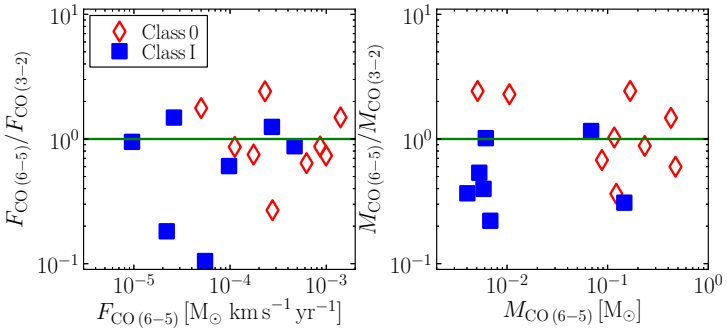

Figure 5.4 – Outflow forces (*left*) and outflow masses (*right*), calculated from CO 6–5 and 3–2 emission are compared for Class 0 and I sources. Green lines are for a ratio of 1.

lobes. The mass is calculated for each channel separately and multiplied by the central velocity of that particular channel. They are then summed and the sum is over all pixels j in the map with outflow emission. This method is formulated as:

$$F_{\rm CO} = c_i \frac{V_{\rm max} \sum_j \left[\int M(V') V' {\rm d}V' \right]_j}{R_{\rm CO}}, \tag{5.4}$$

where $c_{\rm i}$ is the inclination correction, and $R_{\rm CO}$ is the projected size of one of the outflow lobes. These values are computed separately from the CO 3–2 and 6–5 maps of the same source (see Tables 5.1–5.3).

The difference in outflow force between the red and blue outflow lobes ranges from ~1 up to a factor of 10. For sources with a low outflow force this is a result of differences in the inferred outflow mass per lobe, which, in these specific cases, is primarily a result of low S/N. In these cases, the overall uncertainty on the outflow force is high, up to a factor of ten. In other cases, such as HH46 as mentioned above, there is a real asymmetry between the different lobes which is caused by a difference in the surrounding environment. In the following, only the sum of the outflow force as measured from each outflow lobe will be used.

Figure 5.4 shows how the outflow forces and outflow masses calculated from CO 3–2 and 6–5 differ. For strong outflows, there is a factor of a few difference in the two calculations. Interestingly, for both parameters, the values from CO 6–5 are higher in the Class 0 sources but lower in the Class I sources than those from CO 3–2. One possible explanation is that the bright outflows from Class 0 sources suffer more from opacity effects in the 3–2 transition and so the mass is underestimated. Class I sources, on the other hand, generally suffer from low S/N in the 6–5 transition leading to an apparent lower mass. Figure 5.5 displays $F_{\rm CO}$ for Class 0 and Class I sources separately. Generally, Class 0 sources have higher outflow forces and are thus more powerful than their Class I counterparts (Bontemps et al. 1996).

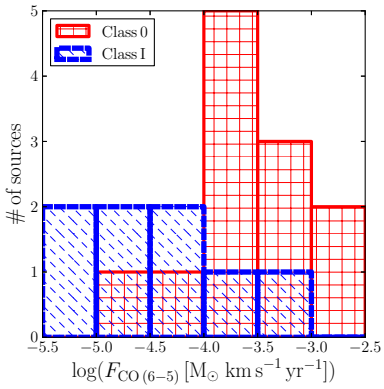

Figure 5.5 – Histograms of calculated total outflow force F_{CO} is shown for Class 0 (red) and Class I (blue) sources.

5.3.3 Other outflow parameters

Other outflow parameters that characterize the outflow activity are the dynamical age, t_{dyn}, outflow mass rate, $\dot{M}_{outflow}$, and kinetic luminosity, L_{kin}.

The dynamical age is determined as

$$t_{dyn} = \frac{R_{CO}}{V_{max}} \,. \tag{5.5}$$

This age is usually also a lower limit on the age of the protostar (Curtis et al. 2010b). The outflow mass loss rate is computed according to

$$\dot{M}_{outflow} = \frac{M_{outflow}}{t_{dyn}} \,. \tag{5.6}$$

The kinetic luminosity is given by

$$L_{kin} = \frac{1}{2} F_{CO} V_{max} \,. \tag{5.7}$$

Outflow parameters derived from the above equations with inclination corrections are presented in Tables 5.1–5.3. Based on the CO 6–5 observations, the strongest outflow emanates from IRAS4A, with the highest value of both outflow force and kinetic luminosity. Other strong outflows include L1448mm, L1157, and BHR71. The results show that outflows have total swept-up masses between ~1 $M_\odot$ (BHR71) to 4×10^{-4} $M_\odot$ (DK Cha), with average mass loss rates between 5×10^{-7} to 7×10^{-5} $M_\odot yr^{-1}$, and outflow forces of 4×10^{-6} to 1×10^{-3} $M_\odot yr^{-1}$ km s^{-1}.

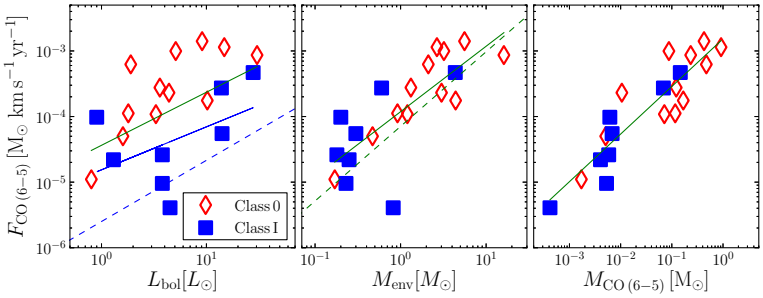

Figure 5.6 – Correlations of $F_{\rm CO}$ with $L_{\rm bol}$, $M_{\rm env}$, and $M_{\rm outflow}$, where $F_{\rm CO}$ is determined from the CO 6–5 data. Red and blue symbols indicate Class 0 and Class I sources, respectively. The green solid line is the fit to all values and the blue solid line is the fit to the Class I sources only. Blue and green dashed lines are the best fits from Bontemps et al. (1996).

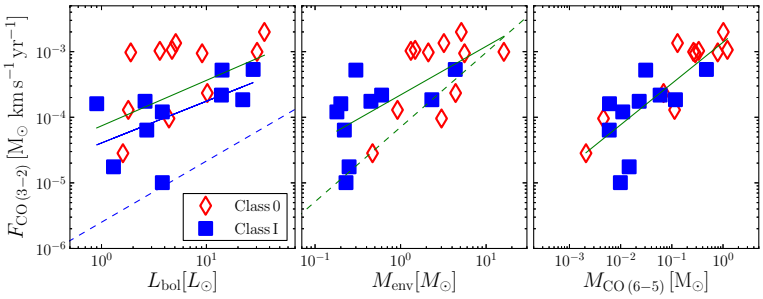

Figure 5.7 – Correlations between $F_{\rm CO}$ as measured from CO 3–2 and bolometric luminosity, envelope mass and outflow mass as determined from CO 6–5.

5.3.4 Correlations

Most previous studies of the outflow force were done using either CO 2–1 or 3–2 (e.g., Cabrit & Bertout 1992, Bontemps et al. 1996, Hogerheijde et al. 1998, Hatchell et al. 2007, van Kempen et al. 2009c). These low-J lines inevitably suffer from opacity effects, but without targeted, deep surveys of, e.g., ^{13}CO, it is difficult to quantify how much the CO column density is underestimated. Furthermore, cloud or envelope emission may contribute to the emission at the lowest outflow velocities at which the bulk of the mass is flowing. With these CO 6–5 observations, some of the above-mentioned issues can be avoided, or their effects can be lessened. In particular, CO 6–5 emission is typically optically thin in the line wings (van Kempen et al. 2009b, Yıldız et al. 2012). Furthermore, the contribution from the surrounding cloud and envelope is much less than for the case of CO 3–2 (Fig. 5.10). Thus, it is important to revisit the correlations of outflow force with bolometric luminosity and envelope mass using these new measurements.

In Fig. 5.6, $F_{\rm CO}$ is plotted against $L_{\rm bol}$, $M_{\rm env}$, and $M_{\rm outflow}$, where the $F_{\rm CO}$ and $M_{\rm outflow}$

values are taken from the CO 6–5 data. The best fit between F_{CO} and L_{bol} is shown with the green line corresponding to

$$\log(F_{CO}) = -(5.02 \pm 0.1) + (0.95 \pm 0.27) \log(L_{bol}) \, . \tag{5.8}$$

Outflows from Class 0 and Class I sources are well-separated; Class 0 sources show more powerful outflows compared to Class I sources of similar luminosity. The Pearson correlation coefficients are r=0.37, 0.42, and 0.68 for all sources, Class 0, and Class I sources, respectively, corresponding to confidences of $\sim$ 2.3, 2.0 and 2.7σ, respectively.

The best fit between F_{CO} and M_{env} is described as

$$\log(F_{CO}) = -(4.37 \pm 0.1) + (1.14 \pm 0.15) \log(M_{env}) \tag{5.9}$$

and Pearson correlation coefficients are r=0.49, 0.39, and 0.66 ($\sim$ 3.1, 1.9 and 2.6σ) for all sources, Class 0, and Class I, respectively. Since early stage Class 0 sources have more envelope mass their outflow force is much higher than for the Class I sources. Only the first correlation appears significant.

Finally, as expected, a strong correlation is found between F_{CO} and $M_{outflow}$ with a Pearson correlation coefficient of r=0.75 for all sources ($\sim$ 4.7σ). The best fit is described as

$$\log(F_{CO}) = -(2.85 \pm 0.1) + (0.77 \pm 0.34) \log(M_{CO}) \, . \tag{5.10}$$

Previously, Bontemps et al. (1996) surveyed 45 sources using CO 2–1 observations with small-scale maps. In Fig. 5.6, the blue and green dashed lines of F_{CO} vs. L_{bol} and M_{env} show the fit results from their Figs. 5 and 6 (Bontemps et al. 1996). Since their number of Class I sources is higher than Class 0 sources, the fit was only done for Class I sources in F_{CO} vs. L_{bol}. In Fig. 5.6, the blue solid line shows the fit for only Class I sources and the correlation is described by,

$$\log(F_{CO}) = -(5.52 \pm 0.1) + (0.87 \pm 0.39) \log(L_{bol}) \, . \tag{5.11}$$

In the F_{CO} vs. M_{env} plot, the fits are shown as green lines for the entire sample. Even though Bontemps et al. (1996) sample is weighted toward lower luminosities, our F_{CO} measurements from CO 6–5 data follow their relation for Class I sources obtained from 2–1 data, but with a shift to higher values of F_{CO}.

Examining the same outflow parameters measured using the CO 3–2 transition, and their correlation with the same outflow parameters, a different picture arises (Fig. 5.7). For the sources in our sample, the correlations follow the same trend but they are all weaker. In particular, the correlations with L_{bol} is at the $\sim$1.5σ level, whereas the correlation with M_{env} is 2.1σ. Although the measured values of, e.g., F_{CO}, fill out the same parameter space as when the measurements are done with CO 6–5, the scatter is larger. The scatter remains of the order of one order of magnitude, which is similar to the scatter reported in the literature (e.g., Bontemps et al. 1996), but because of the limited source sample (20 sources with F_{CO} measurements) it is difficult to compare these 3–2 measurements with what is presented in the literature.

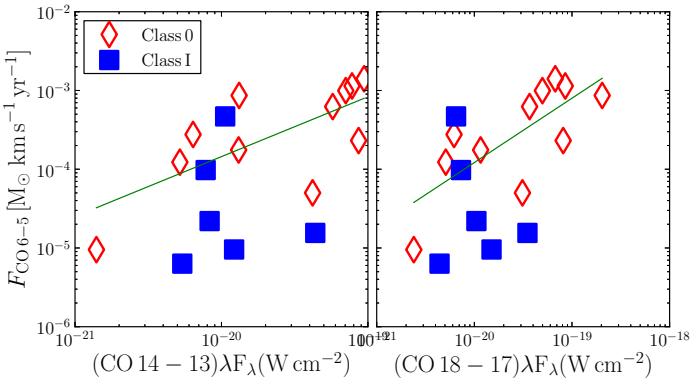

Figure 5.8 – Correlation between F_{CO} and the CO 14–13 and 18–17 fluxes obtained from *Herschel*-PACS.

5.4 Discussion

Our results show that the outflow parameters inferred from the CO 6–5 data show the same trends with L_{bol} and evolutionary stage as found previously in the literature, but with stronger correlations than for the 3–2 data. Even though the same telescope and methods are used for all sources and the spatial resolution is high, there remains a scatter of at least an order of magnitude in the correlation between F_{CO} and L_{bol}. This could point to the importance of "episodic accretion" as a resolution to the "luminosity problem" (Evans et al. 2009, Dunham et al. 2010, 2013). Some Class 0 sources are very luminous, which is likely due to a current rapid burst in accretion which happens every 10^3-10^4 years (Dunham et al. 2010). However, their location in the high state is not constant and would drop in the course of time, on timescales as fast as 10^2 years (Johnstone et al. 2013). The envelope mass, on the other hand, is independent of the current luminosity, and the stronger correlation with M_{env} may simply reflect that more mass is swept up.

Since the outflow force gives the integrated activity over the entire lifetime of YSO, it is also interesting to compare this parameter with the currently shocked gas probed by the *Herschel*-PACS high-*J* CO observations ($J_u > 14$). In Fig. 5.8, F_{CO} is plotted versus CO 14–13 and CO 18–17 fluxes ($E_{up} \sim 580$ and 940 K) obtained from Karska et al. (2013), Goicoechea et al. (2012), Herczeg et al. (2012) and van Kempen et al. (2010a). There is a weak correlation between the CO 18–17 flux and F_{CO} ($r = 0.69 \sim 2.6\sigma$; Fig. 5.8). This correlation illustrates that although CO 18–17 likely traces a different outflow component than CO 6–5 (Santangelo et al. 2012, Nisini et al. 2013, Tafalla et al. 2013), a component closer to the shock front, the underlying driving mechanism is the same. Furthermore, CO 18–17 emission is often extended along the outflow direction (Karska et al. 2013) and clearly traces, spatially, a component related to that traced by CO 6–5. Although the excitation of CO 18–17 requires higher densities and temperatures ($n_{crit} \sim 10^6$

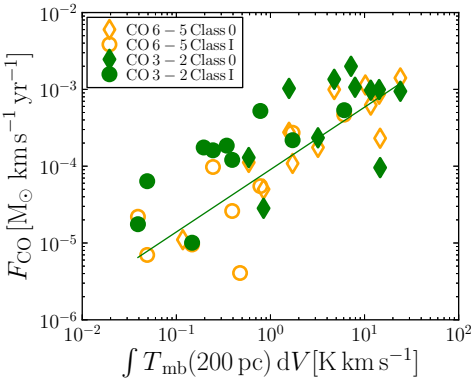

Figure 5.9 – Correlation between F_{CO} measured from the CO 6–5 and CO 3–2 data and the integrated intensity of the ground-state H_2O 1_{10}–1_{01} transition at 557 GHz. The integrated intensities are scaled to a common distance of 200 pc (Kristensen et al. 2012). The correlation is strong, 3.8σ.

cm^{-3}; E_{up} ~ 940 K) than CO 6–5 (n_{crit} ~ 10^5 cm^{-3}; E_{up} ~ 120 K), CO 6–5 likely follows in the wake of the shocks traced by the higher-J lines and therefore the excitation of both lines ultimately depend on the actual shock conditions. Testing this scenario requires velocity-resolved line profiles of high-J lines such as CO 16–15 (Kristensen et al. in prep.).

Another indication that the outflow force as measured from CO 6–5 is more closely linked to the currently shocked gas than 3–2 comes from comparing H_2O and F_{CO}. Water is one of the best shock tracers, as evidenced most recently by several *Herschel* observations (van Kempen et al. 2010b, Lefloch et al. 2010, Nisini et al. 2010, Vasta et al. 2012, Tafalla et al. 2013). Kristensen et al. (2012) compared the integrated intensity of the H_2O 1_{10}–1_{01} transition at 557 GHz with the outflow forces presented in the literature. These observed line intensities are scaled by the square of the source distance to a common distance of d_{avg}=200 pc. The outflow forces were calculated using a variety of methods and data sets, and provided an inhomogeneous sample. No correlation of H_2O integrated intensity with F_{CO} was found. Revisiting this comparison with the newly measured outflow forces reveals a weak correlation with the force measured from CO 3–2 data (2.5σ) and a strong correlation with the force measured from the CO 6–5 data (3.8σ) (Fig. 5.9) (see also Bjerkeli et al. 2012). Thus, F_{CO} as deduced from 6–5 can be used as a measure of the outflow force of the shocked gas, rather than just the entrained, swept-up gas.

5.5 Conclusions

In this chapter, we present large-scale maps of 26 YSOs obtained with the APEX-CHAMP$^+$ instrument (^{12}CO and ^{13}CO 6–5), together with the JCMT-HARP-B instrument (^{12}CO and ^{13}CO 3–2). Our sample consists of deeply embedded Class 0 sources as well as less deeply embedded Class I sources. With these high spatial and spectral resolution maps, we have studied the outflow activity of these two different evolutionary stages

of YSOs in a consistent manner. All embedded sources show large scale outflow activity that can be traced by the CO line wings, however their activity is reduced in the course of evolution to the later evolutionary stages as indicated by several outflow parameters.

One of the key outflow parameters, the outflow force, F_{CO} is quantified and correlations with other physical parameters are sought. In agreement with previous studies, Class 0 sources have higher outflow forces than Class I sources. F_{CO} is directly proportional to M_{env} and $M_{outflow}$, showing that higher outflow forces are associated with higher envelope mass or outflow mass, as present in Class 0 sources. Comparing the outflow force as measured from CO 6–5 data to H_2O observed with *Herschel*-HIFI and high-J CO observed with *Herschel*-PACS reveals a correlation, suggesting that the outflow force from 6–5 is at least weakly related to current shock activity. This is in contrast with the outflow force measured from CO 3–2, where there is little or no correlation with water and these high-J fluxes.

Acknowledgements

UAY is grateful to the APEX and JCMT staff for carrying out the observations. We also thank to NL and MPIfR observers for all APEX observations, Astrochemistry in Leiden is supported by the Netherlands Research School for Astronomy (NOVA), by a Spinoza grant and grant 614.001.008 from the Netherlands Organisation for Scientific Research (NWO), and by the European Community's Seventh Framework Programme FP7/2007-2013 under grant agreement 238258 (LASSIE). Construction of CHAMP$^+$ is a collaboration between the Max-Planck-Institut fur Radioastronomie Bonn, Germany; SRON Netherlands Institute for Space Research, Groningen, the Netherlands; the Netherlands Research School for Astronomy (NOVA); and the Kavli Institute of Nanoscience at Delft University of Technology, the Netherlands; with support from the Netherlands Organization for Scientific Research (NWO) grant 600.063.310.10.

5.6 Additional materials

Table 5.5 – Integration limits and contour levels.

	Blue Lobe[a]			Red Lobe[a]			CO 6–5		CO 3–2	
Source	V_{max} [km s^{-1}]	$V_{out,blue}$ [km s^{-1}]	$V_{in,blue}$ [km s^{-1}]	V_{max} [km s^{-1}]	$V_{in,red}$ [km s^{-1}]	$V_{out,red}$ [km s^{-1}]	Lowest Cntr[b] [K km s^{-1}]	Step Size[b] [K km s^{-1}]	Lowest Cntr[b] [K km s^{-1}]	Step Size[b] [K km s^{-1}]
L1448mm[c]	35.0	−32.0	3.0	37.0	8.0	45.0	...	...	10	10
IRAS2A[c]	23.0	−17.0	6.0	25.0	11.0	36.0	15	20	15	15
IRAS4A	23.1	−15.9	4.0	22.8	9.1	30.0	20	20	20	20
IRAS4B	18.1	−10.9	4.0	15.8	9.1	23.0	20	20	20	20
L1527	8.5	−2.6	4.5	7.1	7.4	13.0	7	4	5	3
Ced110IRS4	7.2	−3.0	3.5	5.8	5.5	10.0	8	5	5	3
BHR71	15.5	−19.9	−6.0	16.4	−3.9	12.0	20	20	...	...
IRAS15398	11.5	−6.4	2.5	10.9	6.6	16.0	5	5	3	3
L483MM	8.5	−3.3	4.0	6.8	6.7	12.0	8	8	5	8
SMM1	17.0	−8.5	6.0	20.5	10.5	29.0	15	20	30	25
SMM4	18.5	−10.5	6.0	12.0	10.5	20.0	15	20	30	25
SMM3	20.1	−12.5	6.0	12.4	10.5	20.0	15	20	30	25
L723MM	13.0	−1.8	9.0	10.8	12.2	22.0	15	10	5	5
B335	12.3	−3.9	6.5	6.6	9.1	15.0	...	...	...	...
L1157[c]	10.4	−7.8	1.5	15.4	3.7	18.0	...	...	10	20
L1489	11.5	−4.3	5.0	6.8	8.7	14.0	3	2	5	10
L1551IRS5[c]	12.7	−6.5	4.5	10.8	7.5	17.0	...	...	10	10
TMR1	9.5	−3.2	4.0	5.7	6.8	12.0	3	3	2	2
TMC1A	15.0	−8.4	4.0	5.4	8.6	12.0	5	5	2	5
TMC1	11.5	−6.3	4.0	14.8	6.7	20.0	4	5	3	3
HH46	11.5	−6.3	4.0	19.8	6.2	25.0	15	8	10	10
DKCha	9.3	−6.2	1.5	8.9	4.3	12.0	5	5	5	5
GSS30IRS1	18.5	−15.0	1.5	16.5	6.0	20.0	20	30	15	15
Elias29	10.8	−6.5	2.5	11.7	6.5	16.0	15	10	7.5	5.0
OphIRS63	8.0	−5.2	1.0	7.2	3.8	10.0	4	1.5	2	1
RNO91	7.5	−7.0	−1.0	5.5	2.0	6.0	3	3	3	3

Notes: [a]Velocity integration limits as shown in Fig. 5.10. [b]Contour levels are given in absolute intensities. [c]Obtained from ^{12}CO 3–2.

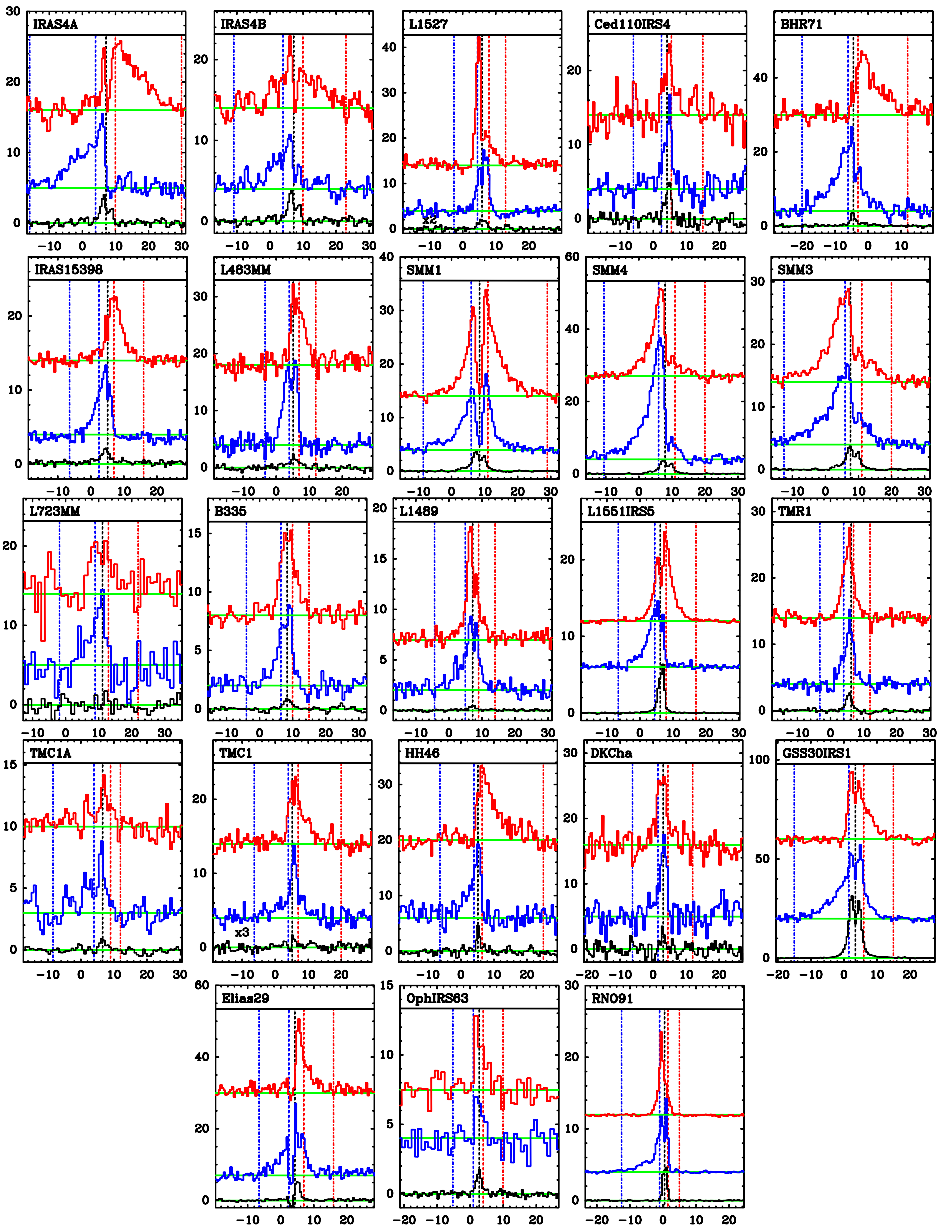

Figure 5.10 – CO 6–5 spectra with selected integration limits indicated. Each panel presents these limits for each source. The black spectrum at the *bottom* is taken from a clean position representative for the envelope emission. The blue spectrum at the *middle* is the representative spectrum from the blue outflow lobe, and red spectrum at the *top* is the representative spectrum from the red outflow lobe. Each panel shows four vertical lines showing the limits, these are $V_{\rm out,blue}$ *(dot-dash blue line)*, $V_{\rm in,blue}$ *(dashed blue line)*, $V_{\rm in,red}$ *(dashed red line)*, and $V_{\rm out,red}$ *(dot-dash red line)*.

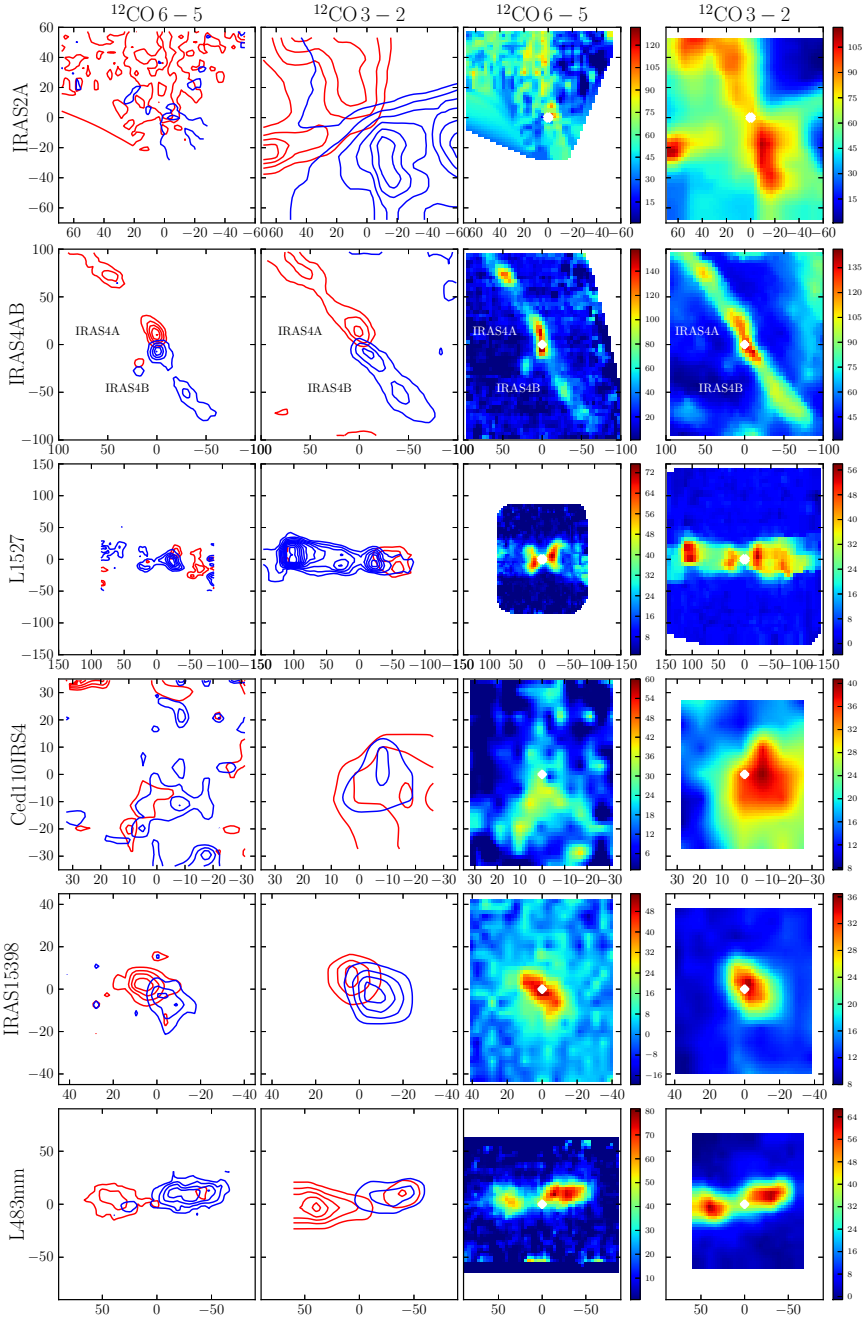

Figure 5.11 – Each row contains contour and integrated intensity maps of sources in ^{12}CO 6–5 and 3–2. The contour levels and integration limits are given in Table 5.5 and integration limits shown in Fig. 5.10.

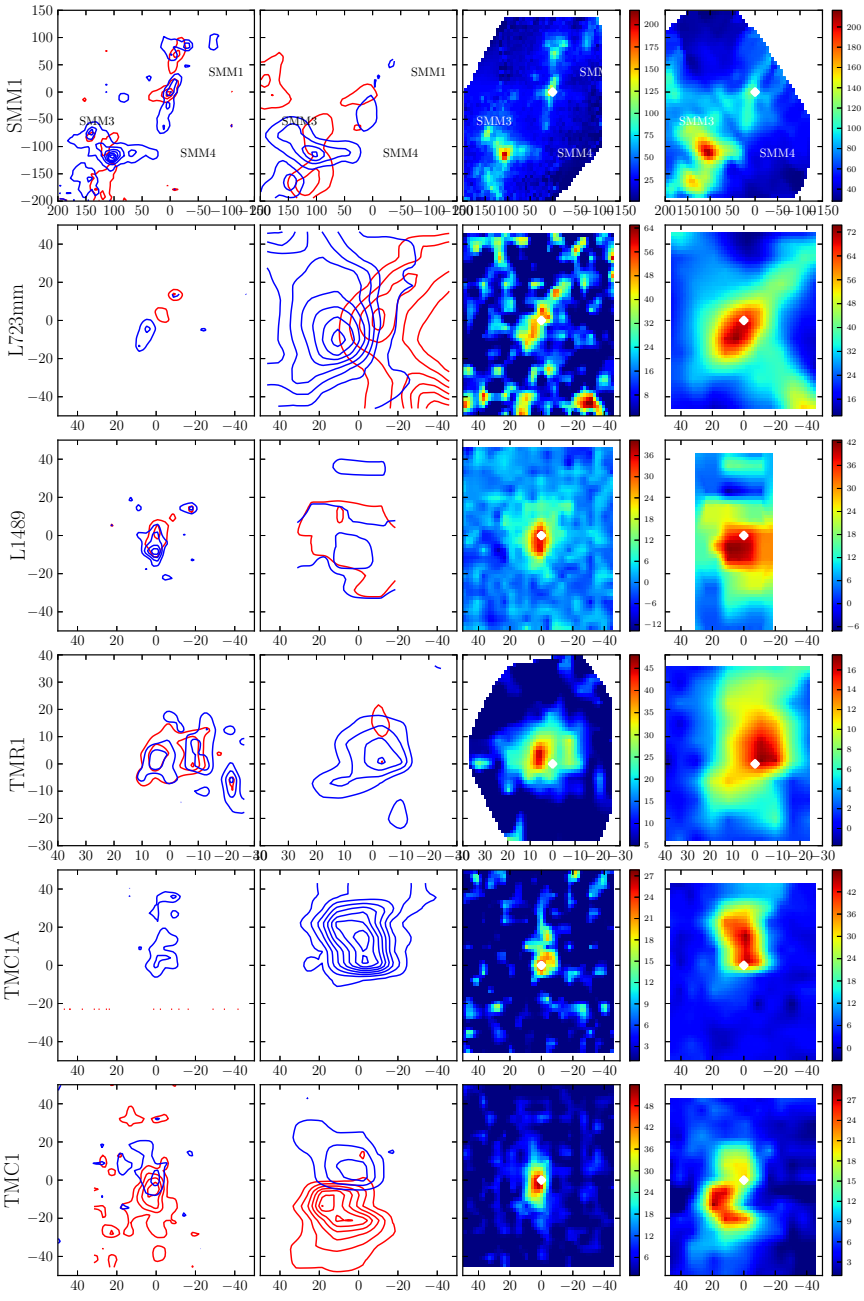

Figure 5.12 – Caption is same as Fig. 5.11.

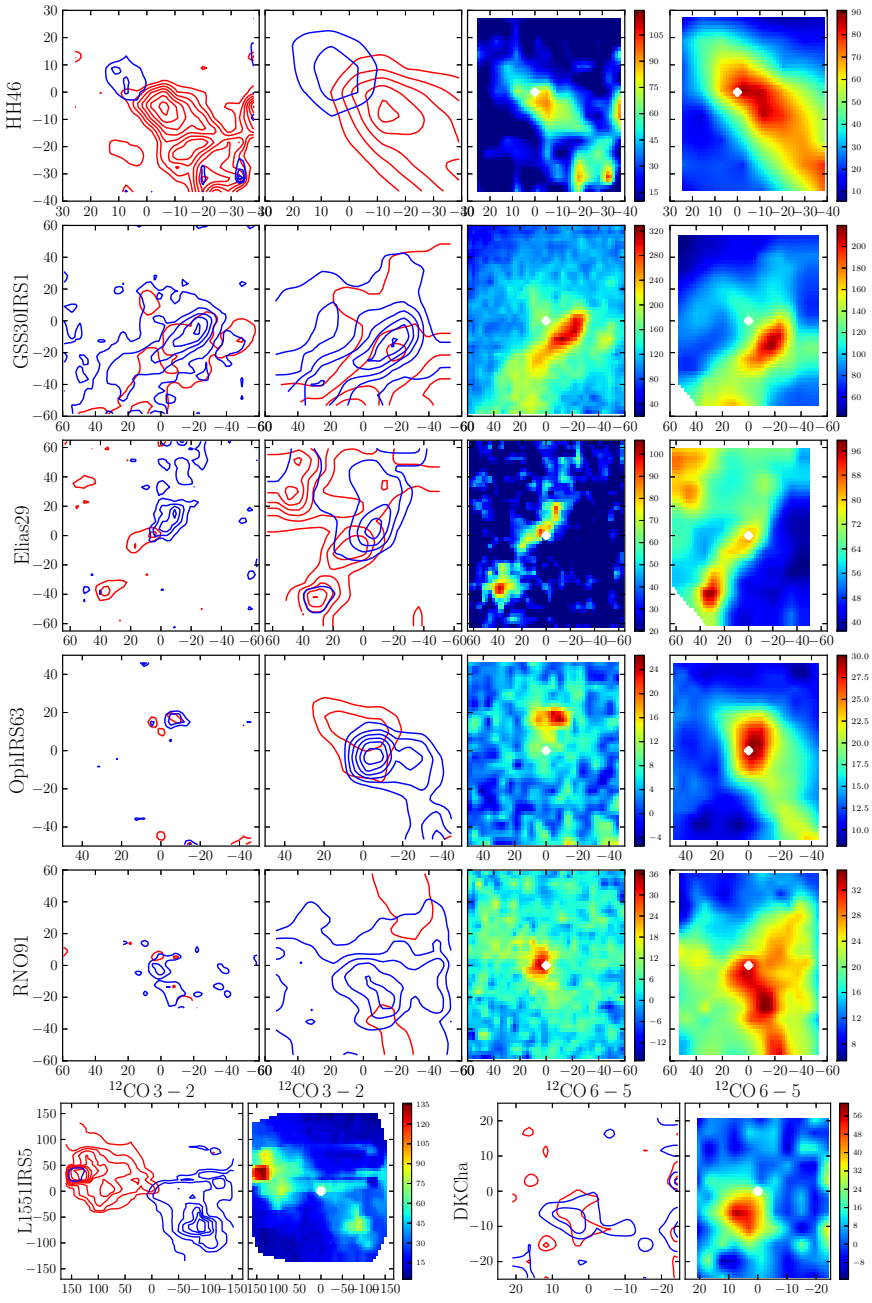

Figure 5.13 – Caption is same as Fig. 5.11.

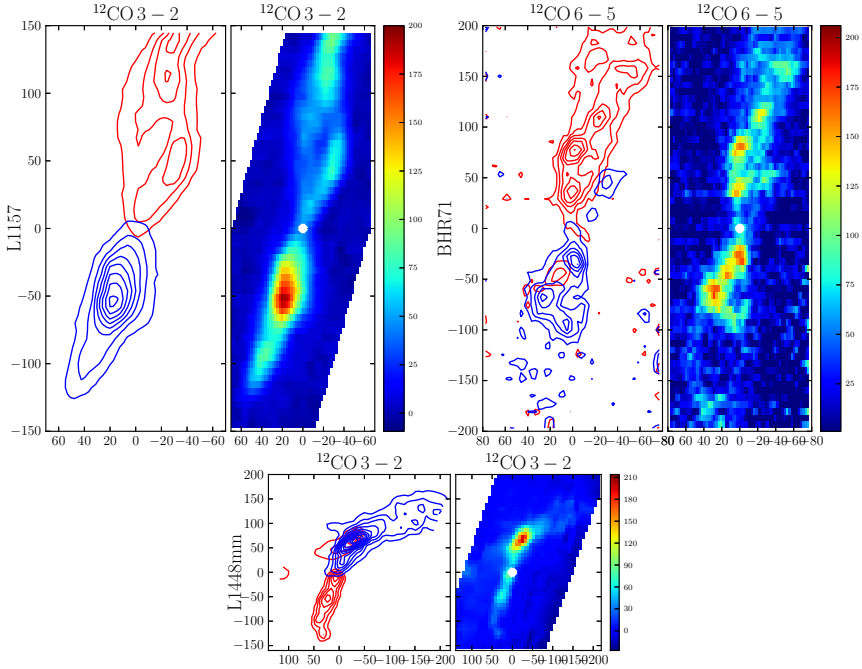

Figure 5.14 – Caption is same as Fig. 5.11.

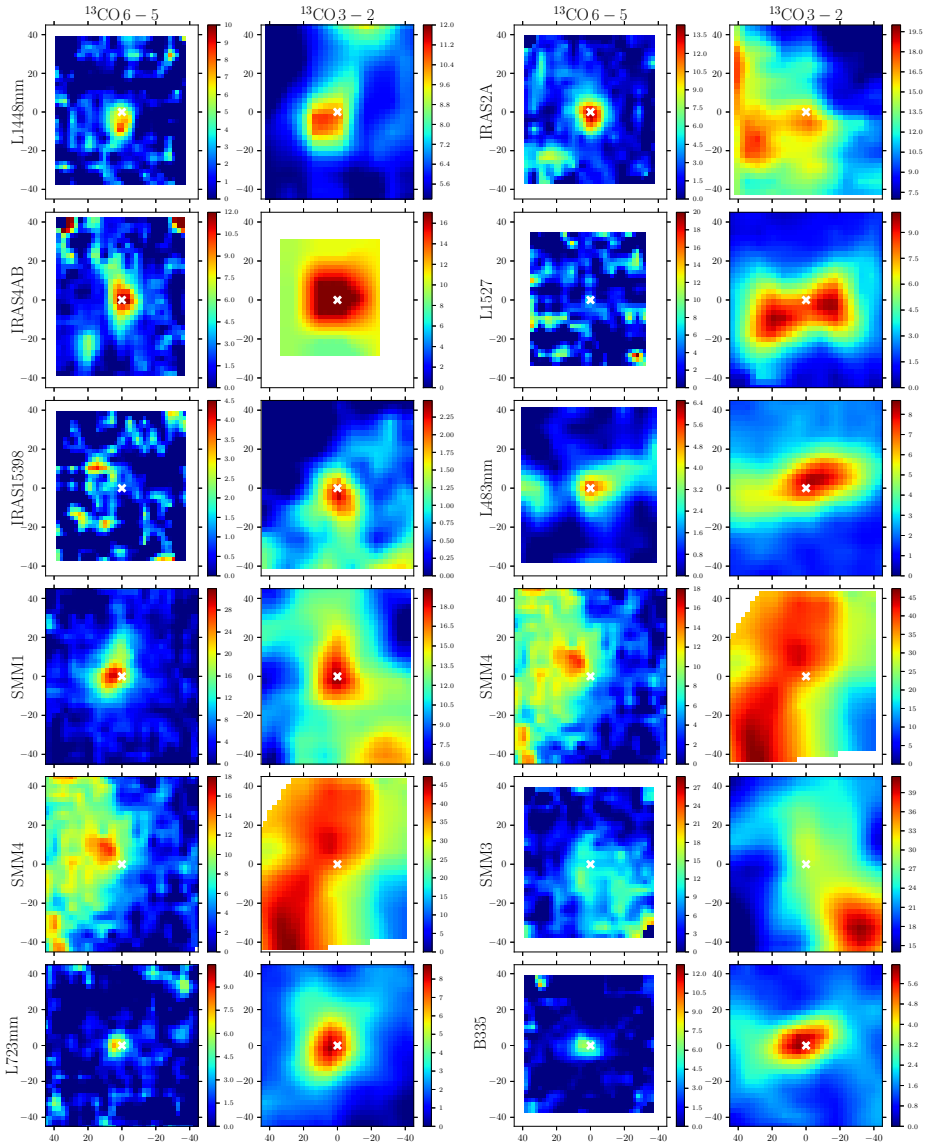

Figure 5.15 – Integrated intensity maps of sources are presented in ^{13}CO 6–5 and 3–2. Integration limits are described in Sect. 5.2.4.

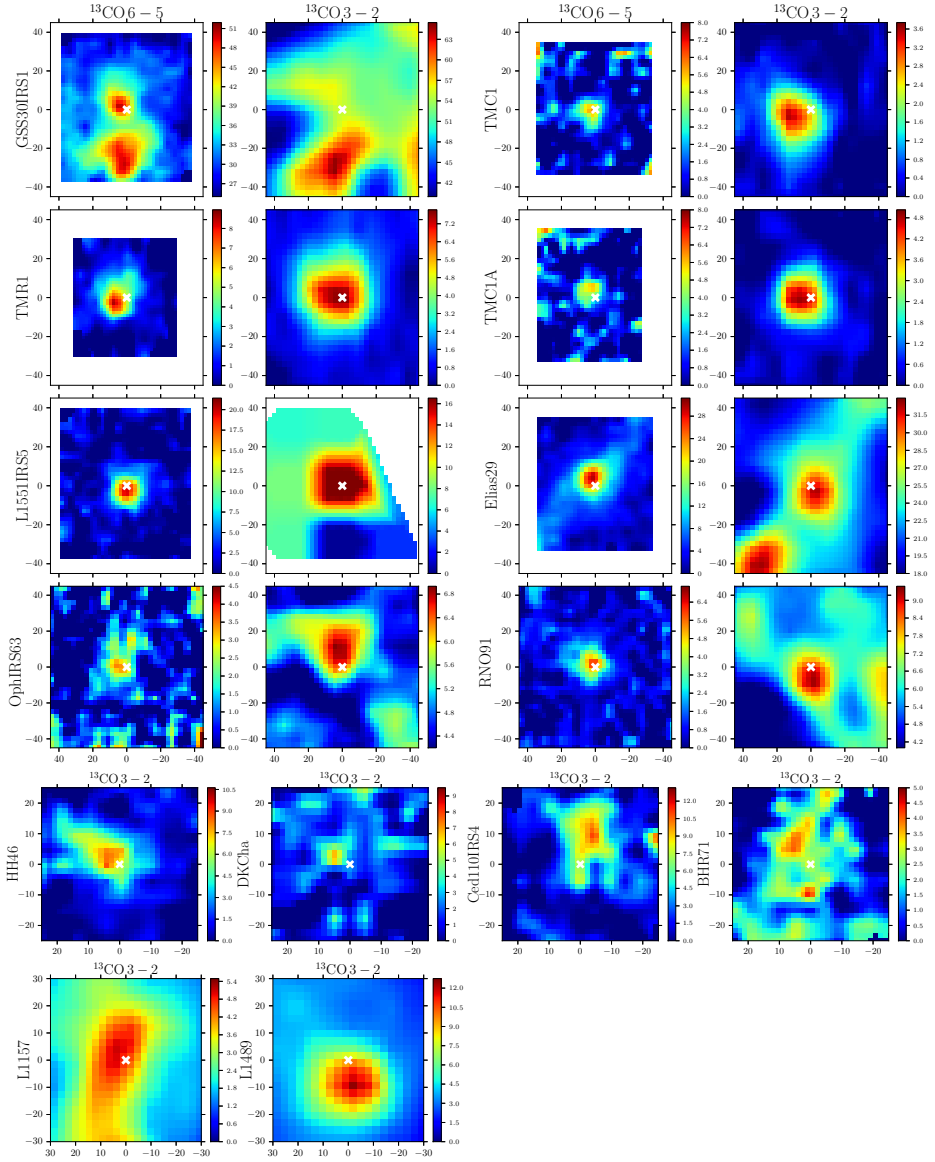

Figure 5.16 – Caption is same as Fig. 5.15.

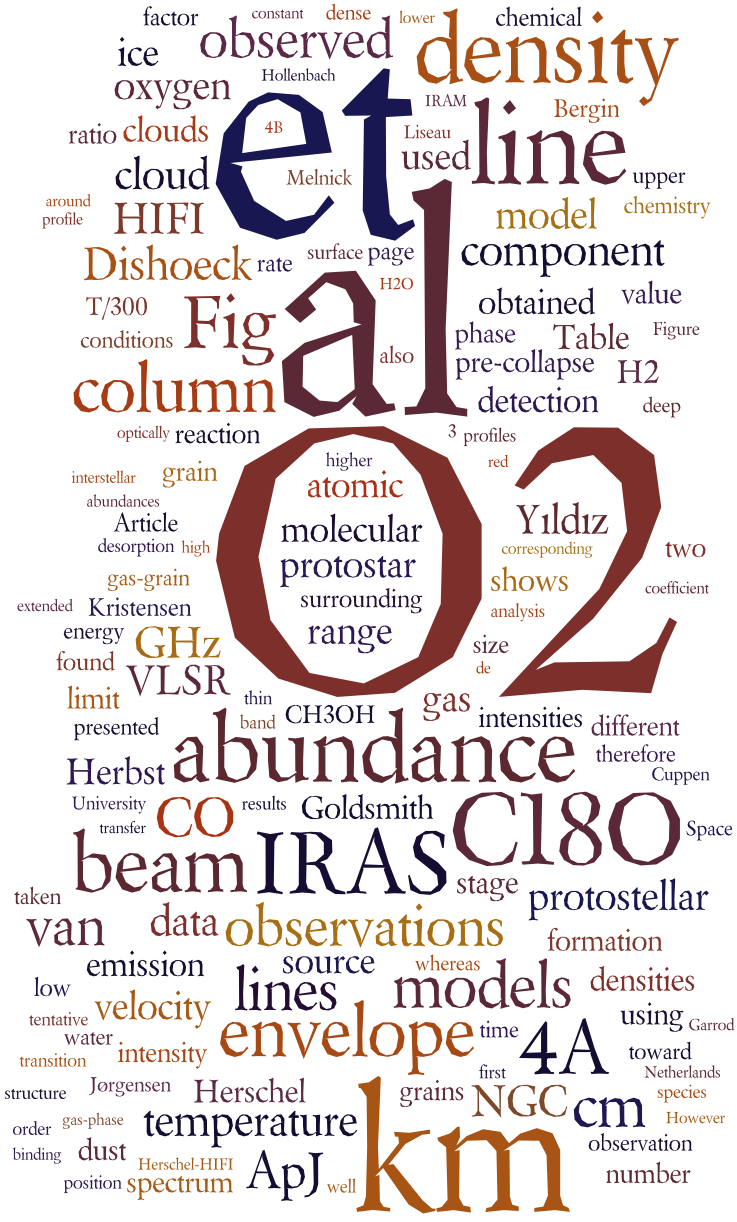
et
al
O2
abundance
density
line
observed
column
Fig
C18O
IRAS
beam
models
envelope
lines
observations
km
4A
cm
NGC
temperature
ApJ
Herschel
dust
spectrum
velocity
emission
source
data
van
protostellar
formation
densities
CO
Herbst
Goldsmith
Yıldız
shows
two
atomic
molecular
protostar
surrounding
range
gas
grain
GHz
VLSR
Kristensen
Article
HIFI
Dishoeck
model
component
obtained
value
Table
Figure
H2
detection
deep
reaction
CH3OH
intensities
different
therefore
Cuppen
Space
Jørgensen
Hollenbach
Melnick
Liseau
Bergin
IRAM
Garrod
Netherlands
Herschel-HIFI
ice
oxygen
cloud
ratio
clouds
factor
constant
dense
lower
chemical
used
upper
chemistry
surface
page
rate
H2O
T/300
conditions
phase
pre-collapse
also
optically
profiles
higher
red
interstellar
abundances
desorption
high
corresponding
gas-grain
extended
energy
found
limit
presented
thin
band
analysis
size
coefficient
University
transfer
results
taken
stage
whereas
low
tentative
water
transition
intensity
time
first
structure
order
binding
position
gas-phase
grains
species
However
observation
number
well
around
profile
4B
2
3
de